# Journal Pre-proof


Mechanical and tribological properties of a refractory high entropy HfMoNbTaTiVWZr thin film metallic glass implanted with nitrogen ions

Karolina Stępniak, Farid Akhtar, Kinga Jasiewicz, Neonila Levintant-Zayonts, Aleksandra Królicka, Dariusz M. Jarząbek

PII: S2238-7854(25)03181-3

DOI: https://doi.org/10.1016/j.jmrt.2025.12.114

Reference: JMRTEC 15881

To appear in: *Journal of Materials Research and Technology*

Received Date: 6 October 2025

Revised Date: 24 November 2025

Accepted Date: 10 December 2025

Please cite this article as: Stępniak K, Akhtar F, Jasiewicz K, Levintant-Zayonts N, Królicka A, Jarząbek DM, Mechanical and tribological properties of a refractory high entropy HfMoNbTaTiVWZr thin film metallic glass implanted with nitrogen ions, *Journal of Materials Research and Technology*, https://doi.org/10.1016/j.jmrt.2025.12.114.

# Mechanical and tribological properties of a refractory high entropy HfMoNbTaTiVWZr thin film metallic glass implanted with nitrogen ions

*Karolina Stępniak[1], Farid Akhtar[2], Kinga Jasiewicz[3], Neonila Levintant-Zayonts[1], Aleksandra Królicka[4,5], Dariusz M. Jarząbek[1,6]**,

[1] Institute of Fundamental Technological Research, Pawińskiego 5B, 02-106 Warsaw, Poland

[2] Luleå University of Technology, Luleå 97187, Sweden

[3] Academic Centre for Materials and Nanotechnology, AGH University of Science and Technology, Aleja Mickiewicza 30, 30-059 Kraków, Poland

[4] Wroclaw University of Science and Technology, Department of Metal Forming, Welding and Metrology, Wybrzeże Wyspiańskiego 27, 50-370 Wroclaw, Poland

[5] Centre of Materials Science and Metal Forming, Wrocław University of Science and Technology, Łukasiewicza 5, 50-351 Wrocław, Poland

[6] Warsaw University of Technology, Faculty of Mechatronics, św. Andrzeja Boboli 8, 02-525 Warsaw, Poland

*Corresponding Author: Dariusz Jarząbek, e-mail: djarz@ippt.pan.pl, Adress: Institute of Fundamental Technological Research, Pawińskiego 5B, 02-106 Warsaw, Poland

E-mail addresses: kstep@ippt.pan.pl (K. Stępniak), farid.akhtar@ltu.se (F. Akhtar), kjasiewicz@agh.edu.pl (K. Jasiewicz), neonila@ippt.pan.pl (N. Levintant-Zayonts), aleksandra.krolicka@pwr.edu.pl (A. Królicka), djarz@ippt.pan.pl (D. Jarząbek)

**Abstract**

This study examines nitrogen ion implantation's effects on the microstructure, mechanical behavior, and tribological performance of an octonary high-entropy thin film metallic glass HfMoNbTaTiVWZr. Ion implantation led to binary nitride formation, elemental redistribution, and surface modifications while maintaining significant degree of amorphization, what indicates local atomic rearrangement rather than crystallization. Structural and chemical analyses using TEM, XRD, and EDS mapping revealed phase stability changes and preferential segregation of heavy elements like hafnium and tantalum at high doses. Hardness enhancement was attributed to solid solution strengthening, fine nitride formation, increased lattice distortion, residual stress, and densification. At an optimal implantation dose (1e17

ions/cm²), hardness increased to 20 GPa, reducing the coefficient of friction and improving wear resistance. A comparison with a magnetron-sputtered (HfMoNbTaTiVWZr)N thin film showed distinct hardness-depth profiles, confirming localized strengthening effects. These findings highlight nitrogen implantation as an effective surface engineering technique for optimizing material performance in demanding applications.

**Keywords**

High entropy film metallic glasses; Ion implantation; Microstructure; Indentation; Surface characteristics

## 1. Introduction

High entropy metallic glasses (HEMGs) represent a novel class of materials that combine the inherent properties of metallic glasses - such as high strength and irradiation resistance - with the compositional complexity arising from large number of constituent elements [1]. Compositionally complex systems of refractory high entropy metallic glasses (RHEMGs) are particularly interesting due to their exceptional thermal stability, oxidation resistance and mechanical performance at elevated temperatures [2]. These materials have garnered significant attention recently due to their potential applications in extreme environments, including high temperatures, aggressive chemical media, nuclear power plants and tribological systems [1–3]. Previous studies have extensively examined various aspects such as thermal crystallization kinetics, compositional and structural characteristics, mechanical attributes, fracture behavior, preparation techniques and glass-forming abilities [4,5]. For example, studies have elucidated the thermal crystallization kinetics of RHEMGs, revealing pathways to enhance their stability during high-temperature applications [6]. Furthermore, research on compositional and structural properties of RHEMGs has identified potential, optimal combinations of elements to achieve superior strength and ductility [7]. Recent studies on lightweight refractory medium-entropy alloys have demonstrated that controlled compositional tuning and microstructural engineering can significantly enhance room-temperature ductility and formability, highlighting the importance of atomistic-level design strategies for refractory systems [8,9].

While the bulk properties of RHEMGs are undoubtedly promising, it is often the surface of these materials that must meet additional, application-specific requirements. In many cases, particularly for metallic glasses, the surface layer needs to exhibit enhanced hardness, improved corrosion resistance, low friction coefficient and increased wear resistance to perform reliably in demanding environments. One effective strategy to achieve such surface modifications without compromising the advantageous amorphous structure of metallic glasses is ion implantation. This technique allows for the formation of a modified surface layer that is intrinsically bonded to the substrate, thereby eliminating issues related to adhesion that are common in coating-based approaches. Moreover, ion implantation can tailor the surface properties while preserving the amorphous character of the material, which is critical for

maintaining its unique combination of mechanical and chemical attributes. It should be noted that, in this technique, energetic ions are accelerated toward a solid surface using an electric field, enabling their penetration into the near-surface region of the material. It allows precise control over the implanted ion species, energy, and fluence, making it a powerful tool for modifying surface chemistry, structure, and properties without altering the bulk. Figure 1 presents a simplified schematic of the ion implantation process, where nitrogen ions are extracted from an ion source, accelerated and implanted into the material, forming a modified layer with altered bonding, hardness and chemical stability. Ion implantation can also induce amorphization in crystalline materials, drawing intriguing parallels with the glass formation process itself [10]. Given these similarities, investigating ion implantation in the context of RHEMGs could provide new insights into their structural stability and surface optimization.

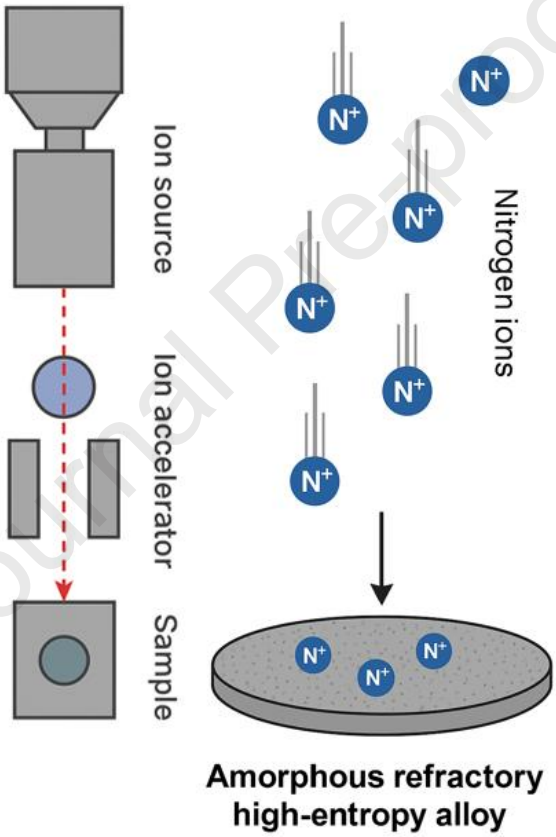


*Figure 1. Schematic illustration of nitrogen ion implantation into an amorphous refractory high-entropy alloy. The process involves ion extraction, acceleration and incorporation into the near-surface region of the target material.*

In conventional metallic glasses, it has been already shown that ion implantation can significantly enhance hardness, wear and oxidation resistance. For example, Tao et al. observed an increase in hardness and thermal stability of ZrCuNiAl after Co ions implantation [11]. On the other hand, studies have reported that especially the implantation of nitrogen ions leads to formation of hard phases or interstitial compounds, significantly enhancing surface hardness and reducing wear rates of high entropy alloys. Jenczyk et al. [12] investigated nitrogen ion implanted $AlCoCrFeNiTi_{0.2}$ high-

entropy alloy using high ion doses, which resulted in an unexpected X-ray diffraction (XRD) spectrum with unidentified peaks, which can be attributed to high entropy ceramics formation. An improved wear resistance as well as hardness of the samples were observed with the increase of the ion dose during implantation. The enhanced wear resistance after implantation was also confirmed by Pogrebnjak et al. [13] who conducted their research on high entropy alloy nitride (TiHfZrNbVTa)N coatings. Authors state that the presence of Nb atoms could favor the formation of solid solution with FCC structure in multielement HEA nitride which they confirmed using first principles calculation. All these findings are particularly significant for applications requiring precise tailoring of surface properties while maintaining the properties of the bulk material.

Despite these advancements, the combined field of RHEMGs and ion implantation remains largely underexplored. Few studies have explored how implanted ions influence the inherently disordered atomic structure of metallic glasses, particularly in RHEAs, where this disorder is further compounded by compositional complexity [14]. Nevertheless, this interplay still remains scarcely investigated, leaving a gap in our understanding of ion interactions in such materials. Especially, nitrogen implantation can induce significant changes in the local atomic and lattice structure, potentially leading to the formation of nitrides, densification or alterations in bonding configurations. These changes may profoundly affect the mechanical, tribological, and chemical performance of the material. Key areas such as nitrogen diffusion mechanisms, potential nitride formation, and their effects on mechanical and tribological properties are yet to be fully understood. For instance, the interaction between nitrogen and the multi-principal element lattice may result in unique bonding configurations, potentially creating novel phases, i.e. high entropy nitrides, with enhanced properties [14,15].

Hence, this study focuses on the effect of nitrogen ion implantation on a thin film of the high entropy metallic glass HfMoNbTaTiVWZr, which is derived from the family of refractory high entropy alloys. This alloy was selected due to its exceptional compositional complexity, high thermal and mechanical stability and promising resistance to radiation damage. The use of eight refractory elements introduces significant atomic-level disorder and results in high configurational entropy, which promotes glass formation and suppresses crystallization during deposition and subsequent treatments. Our previous work [14] has shown that this amorphous thin film metallic glass exhibits remarkable radiation resistance, as implantation with non-reactive argon ions caused negligible changes in hardness or fracture behavior. In contrast, the corresponding nitride (HfMoNbTaTiVWZr)N, although exhibiting superhardness (~30 GPa), demonstrated a measurable decrease in mechanical stability after irradiation. Therefore, the present study explores nitrogen ion implantation as a method to locally enhance surface hardness via nitride precipitation, while preserving the amorphous structure that is presumably responsible for the material's radiation tolerance. This combination makes the system especially attractive for applications in extreme environments such as high-temperature tribology, nuclear energy systems and advanced microelectronic components.

## 2. Experimental

### 2.1. Sample preparation

In this study, thin film with the thickness around 1 μm of an octonary high entropy compositionally complex metallic glass HfMoNbTaTiVWZr was manufactured on a silicon substrate using magnetron sputtering deposition method. In the process a partially sintered target was used, for full details refer to ref [14]. Next, three samples were implanted with nitrogen ions at a beam energy of 60 keV, using fluences of $d_1$=2e16, $d_2$=1e17 and $d_3$=1e18 ions/cm². Before implantation, the samples were meticulously cleaned with ethanol and acetone to remove any residual organic contamination. All ion beam implantation experiments were conducted at room temperature under a chamber pressure of $2\times10^{-5}$ hPa. The samples were mounted on a thick steel plate positioned perpendicular to the nitrogen beam. Temperature monitoring was conducted for the sample implanted with a fluence of 1e18 ions/cm². A thermocouple, placed in contact with the sample's bottom surface, recorded the temperature. During irradiation, the temperature of this sample rose within the first 35 minutes, stabilizing between 130 °C and 135 °C for the remainder of the 3.5-hour implantation. The ion implantation process is automatically controlled by control system, equipped with a complex sof- and hard-ware module designed to measure current through the sample (which ranged from 0.4 mA to 0.6 mA ) and the total ion beam current, as well as perform ion beam diagnostics within the focusing system. It is a separate component of the ion implanter and consists of: 1) an electromechanical measuring head-system (including the measuring grid used to current measure); 2) a specialized 16-channel current converter card, used to convert the current flowing in the tungsten electrodes of the measuring grid, induced by the beam, to voltage levels appropriate for the analog-to-digital card; 3) a 16-channel analog-to-digital card; 4) a program for complete carrying out the implantation process, as well as to control of analog-to-digital cards, current converter, and the entire control system.

The implantation energy of 60 keV was selected on the basis of Stopping and Range of Ions in Matter (SRIM) simulations to ensure that nitrogen ions do not penetrate deeper than approximately 10% of the total film thickness (~1 μm). The simulation results indicated that the maximum damage peak (maximum displacements per atom (dpa)) occurs at depths below ~100 nm, which guarantees that the implanted region is fully confined within the coating. This choice is particularly important for nanoindentation: by restricting implantation to the upper part of the film, the measured hardness and modulus are not affected by the silicon substrate and reflect only the response of the modified material. The applied fluence range ($2\times10^{16}$ to $1\times10^{18}$ ions/cm²) was selected to span the transition from low-dose defect generation to nitride formation and, at the highest dose, to implantation-induced structural degradation, allowing identification of the optimal dose window for mechanical property enhancement.

To calculate dpa and ion ranges with the use of SRIM results the following formula was used [16]:

$$dpa = \frac{\Phi(\frac{ions}{cm^2}) \times \gamma}{N} \quad (1)$$

where Φ is the implantation fluence, $\gamma$ is the number of displacements produced by a primary knock-on atom (PKA), which can be found in the TRIM (Transport of Ions in Matter) output file (VACANCY.TXT, Vacancies by recoils), and $N$ is the atomic density. Density of investigated alloy was estimated using ThermoCalc software with TCHEA7 database.

Surface morphology was investigated with scanning electron microscope (SEM) - Zeiss Crossbeam 350 equipped with energy dispersive X-ray spectroscopy (EDS) detector. Both EDS spectra and elemental maps were collected from random places of the samples. EDS data was analyzed with the help of EDAX TEAM software. Surface properties – adhesion and roughness - were determined using a FlexAFM atomic force microscope (AFM) from Nanosurf AG, equipped with a HQ:CSC17/AI BS probe. Prior to the experiments, calibration for normal force was performed using the Sader method [17]. Topography images were acquired over a scan area of 10 × 10 μm in the contact mode. The average surface roughness (Ra) was calculated using Gwyddion software based on raw topography images. The adhesion force between the tip and the sample was measured using the standard AFM force-distance curve technique by extracting the pull-off force values [18]. All data were processed and analyzed using both the native Nanosurf software and Gwyddion for topography evaluation.

### 2.2. Microstructure and phase composition

Atomic structure was determined using both experimental and theoretical methods. The crystalline structures of the specimens were identified by using the Empyrean PANAlytical diffractometer with the Rietveld analysis. The diffraction experiment was performed with grazing incidence geometry to ensure a constant penetration depth of the incident X-ray beam. All measurements were realized with Cu-$K_{\alpha 1}$ radiation with a wavelength of $\lambda$= 1.540598 Å. For measurements, capillary optics were used which ensured a quasi-parallel incident beam. The diffraction data were acquired with a Pixcel1D-Medipix3 detector. The 2H values detected during the experiment were 20 - 105°, with a step size of 0.026°; the measurement lasted approximately 10 h. The incident angle was constant (2.1°). Providing such a low angle of incidence of the X-ray beam with respect to the surface of the implanted samples made it possible to carry out measurements from a small surface sample volume. This approach was chosen because the implantation process was expected to affect only depths below 200 nm.

189 The material exhibited an amorphous structure so the amount of this phase was determined for the
190 implanted samples using Match! 3 software. To analyze the obtained diffractograms, theoretical
191 calculations were performed for both the high-entropy nitride and binary nitrides to evaluate the
192 potential formation of crystalline phases. Although the pristine RHEMG was amorphous, its atomic
193 structure could be modified through nitrogen ion implantation. The first step of theoretical analysis was
194 establishing the lattice constant of hypothetical (TaNbHfZrTiMoWV)N using Vegard's rule of mixture
195 [19]:

$$a_{nitride} = \sum_i c_i a_i \tag{2}$$

196 where $a_i$ is lattice constant of binary nitride of i-th constituent element of considered RHEMG and $c_i$ is
197 concentration. Most of those elements forms nitrides with NaCl-type structure, except MoN and WN
198 (Table 1). For those two systems, theoretical lattice constants had to be used [20]. The lattice constant
199 of the hypothetical (TaNbHfZrTiMoWV)N nitride was estimated calculated to be approximately 4.33Å.
200 Theoretical XRD pattern of such high entropy nitride was generated using the VESTA software and
201 compared to the experimental diffractograms. The same scheme of generating XRD patterns and
202 comparison with available experimental data was performed for simple binary nitrides and more
203 complex structures found in Materials Project database [21].

204 *Table 1. Lattice constants of binary nitrides*

| | Ta | Nb | Hf | Zr | Ti | V | Mo | W |
|---|---|---|---|---|---|---|---|---|
| **a [Å]** | 4.33 | 4.39 | 4.52 | 4.59 | 4.24 | 4.14 | 4.25 | 4.20 |

205

206 To analyze the microstructure of cross sections thin lamellas were produced using focused ion
207 beam (FIB) milling in SEM microscope Zeiss Crossbeam 350. The samples prepared in this way were
208 examined using transmission electron microscope (TEM) TALOS F200X with X-FEG field emission
209 cathode equipped with a four-detector windowless Super X EDS system characterized by an extremely
210 large detection area. TEM and HAADF (high-angle annular dark-field) images, EDS spectra, elemental
211 distribution maps and SAED were obtained.

212

213 **2.3. Mechanical and wear resistance tests**

214 Multi-cycle indentation was applied to obtain the depth profiles of the hardness changes. The
215 tests were performed on the Ultra Nanoindentation Tester (UNHT Anton Paar) equipped with a
216 Berkovich tip. On each sample, 21 cycles from 0.1 to 10 mN were performed with the load control and
217 constant strain rate equal to approximately $0.01 s^{-1}$. Each cycle began when the unloading force reached

0.05 mN. This approach generated hardness measurements for the same location at increasing depths. The maximum depth of indentation ranged from 160 nm to 250 nm, depending on the hardness of the specimen. Hardness and indentation depth were calculated from the unloading curve with the Oliver-Pharr method [22], ignoring the top 5% and bottom 30% of the unloading curve for model fitting.

Wear resistance of the samples were estimated with a scratch test method. The measurements were performed with the use of Micro Combi Tester MCT3 equipped with a spheroconical diamond Rockwell C tip with a radius of 100 µm. Tests were conducted with the increasing load form 30 mN to 3000 mN and a scratch speed of 6 mm/min, each scratch was 2 mm long. Microscope images of scratches were taken using the optical module in the device.

Nanoindentation toughness ($K_{IC}$) measurement was performed in-situ using an Alemnis Nanoindenter equipped with a cube-corner tip. The experiments were carried out with the maximum load ($F_m$) of 20 mN. After the tests, the imprints were imaged using SEM (Zeiss Crossbeam 350), and for the those for whom cracks have appeared the average crack lengths – c, were precisely measured. To determine the nanoindentation toughness of brittle materials, the following formula was used [23,24]:

$$K_{IC} = \delta\left(\frac{E}{H}\right)^{1/2} \frac{F_m}{c^{3/2}} \quad (3)$$

The elastic modulus $E$ and hardness $H$ were measured and determined during multi-cycle indentation, $\delta$ is an empirical constant which depends on the geometry of the indenter, for the indenter used, a value of 0.036 was assumed [24].

## 3. Results

### 3.1. Ion implantation

SRIM calculations provided information about ion ranges and dpa in relation to ion doses and depth of penetration. The average ions range is equal to 606 Å but some ions penetrate RHEMG layer even up to a depth of approximately 150 nm (Fig. 2a). Maximum dpa is obtained at around 50 nm of depth and its value $dpa_{max}$ for $d_1$ dose is approximately 2, for $d_2$ ~10 and for $d_3$ ~100 (Fig. 2b). Relatively low ion range is caused mainly by high density of the investigated material ($\rho = 12.26$ g/cm$^3$).

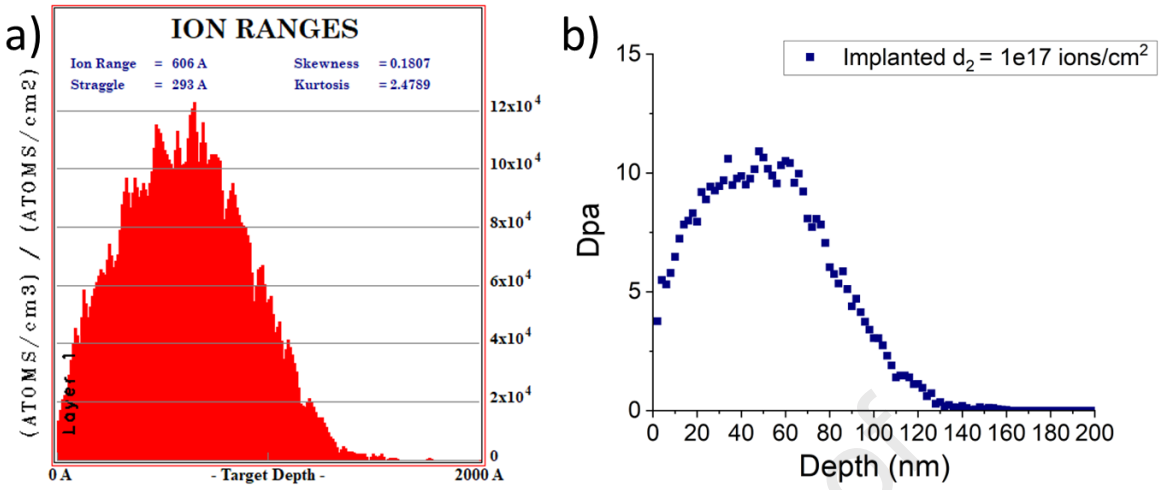


*Figure 2. (a) SRIM calculation and histogram of ion range during ion implantation b) dpa as a function of penetration depth for 1e17 ions/cm² dose.*

### 3.2. Surface characteristics

In our previous paper [14] it was shown that all the constituent elements of the alloy are uniformly distributed in the coating. The virgin alloy composition measured with energy dispersive X-ray spectroscopy (EDS) is shown in Table 2.

*Table 2. Chemical composition of investigated RHEMG.*

| Element | Hf | Nb | Mo | Ta | Ti | V | W | Zr |
|---|---|---|---|---|---|---|---|---|
| atomic % | 10.24 | 11.72 | 13.22 | 13.58 | 13.19 | 17.7 | 13.27 | 7.08 |
| weight % | 16.23 | 9.67 | 11.26 | 21.82 | 5.61 | 8.01 | 21.66 | 5.73 |

Furthermore, the EDS spectra presented in Fig. 4 show that the non-implanted sample exhibits no detectable N-Kα peak (Fig. 4a), whereas clear and progressively stronger nitrogen peaks appear for samples implanted with increasing fluence (Fig. 4b-d). The increase in peak intensity correlates directly with the quantitative nitrogen contents listed in Table 3: approximately 2.3 at.% N for $2\times10^{16}$ ions/cm², 35 at.% N for $1\times10^{17}$ ions/cm², and 56.8 at.% N for $1\times10^{18}$ ions/cm². While EDS provides only semi-quantitative estimates in thin films, the combined spectral evolution and measured compositions consistently confirm the systematic incorporation of nitrogen into the near-surface region.

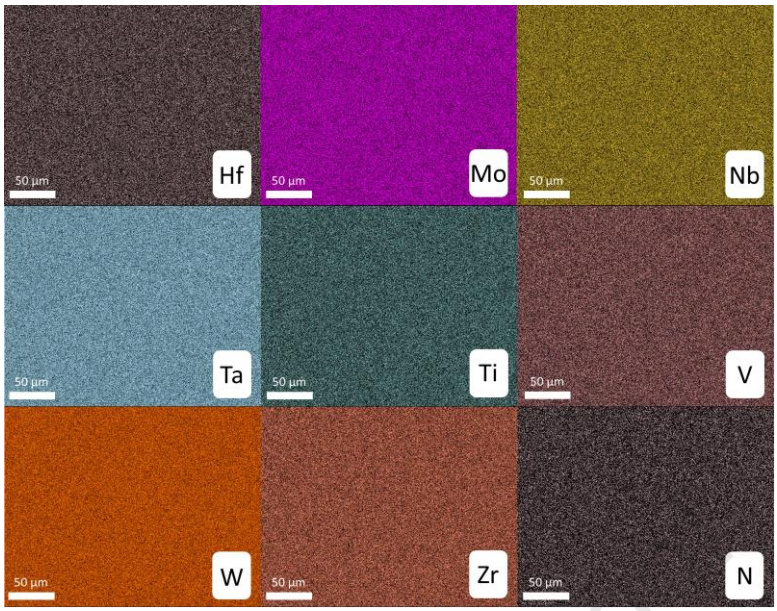


*Figure 3. EDS Map - Element distribution on the surface of the sample implanted with dose $d_2$=1e17 ions/cm$^2$.*

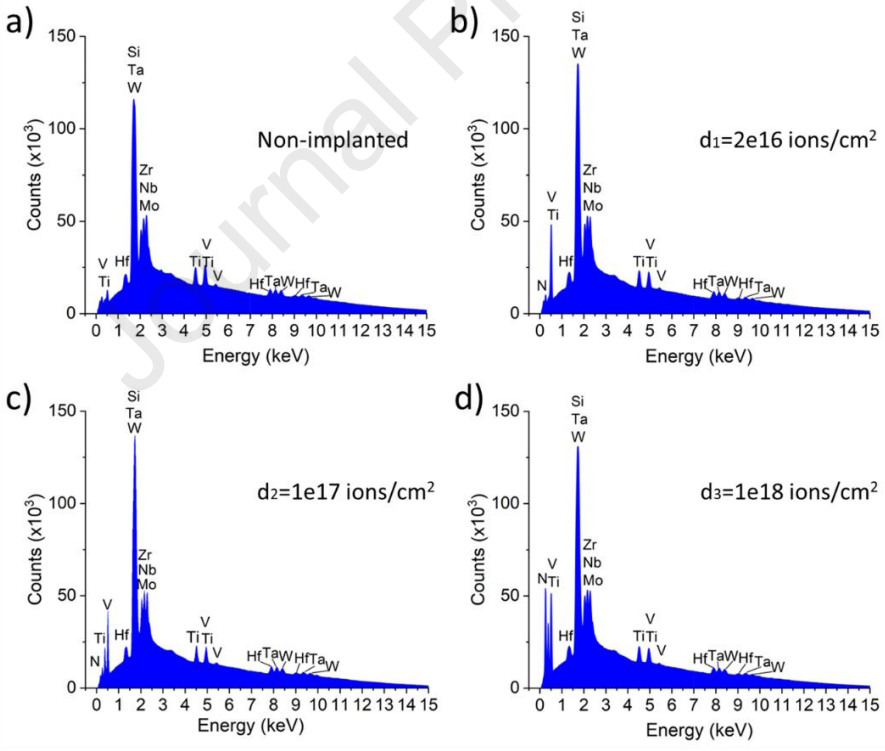


*Figure 4. EDS spectra of a) non-implanted, b) implanted with $d_1$ dose c) implanted with $d_2$ dose d) implanted with $d_3$ dose samples; results obtained on the surface of each sample.*

*Table 2. Nitrogen content in implanted samples measured with EDS.*

| Ion dose [ions/cm$^2$] | Nitrogen content | |
|---|---|---|
| | Weight % | Atomic % |
| **2e16** | **0.3** | **2.3** |
| **1e17** | **6.1** | **35.0** |
| **1e18** | **15.1** | **56.8** |

Results of AFM measurements (Table 4, Fig. 5 and 6) show that surface roughness does not change significantly under the influence of ion implantation until the highest dose is applied. Only for the sample implanted with the dose $d_3$, there is an increase in $R_a$ compared to the other samples. It is a classical effect - ion implantation alters surface roughness due to the high-energy bombardment of ions onto the material's surface. This process creates localized damage, displaces atoms, and introduces point defects, causing changes in the microstructure and a modification of the surface morphology, often increasing its roughness [25]. As the ion dose increases, more ions penetrate the surface, intensifying these effects. Higher doses lead to greater atomic displacement and defect accumulation, which can cause surface swelling, blistering or the formation of micro-rough structures, further increasing the surface roughness.

Moreover, the tip - surface adhesion measured by AFM decreases with increasing ion dose (Fig. 6). This pull-off force reflects the interaction between the silicon AFM probe and the outermost atomic layers of the coating; therefore, it is sensitive only to implantation-induced changes within the modified near-surface region. The reduction in tip-surface adhesion can be attributed to changes in surface chemistry, including nitrogen incorporation, reduced density of dangling bonds [26], and possible nitride formation, all of which lower the surface energy.

*Table 3. Surface roughness ($R_a$) of investigated samples.*

| Sample | Non-implanted | Implanted $d_1$=2e16 ions/cm$^2$ | Implanted $d_2$=1e17 ions/cm$^2$ | Implanted $d_3$=1e18 ions/cm$^2$ |
|---|---|---|---|---|
| $R_a$[nm] | **1.03±0.33** | **1.3±0.1** | **1.11±0.18** | **5.39±0.18** |

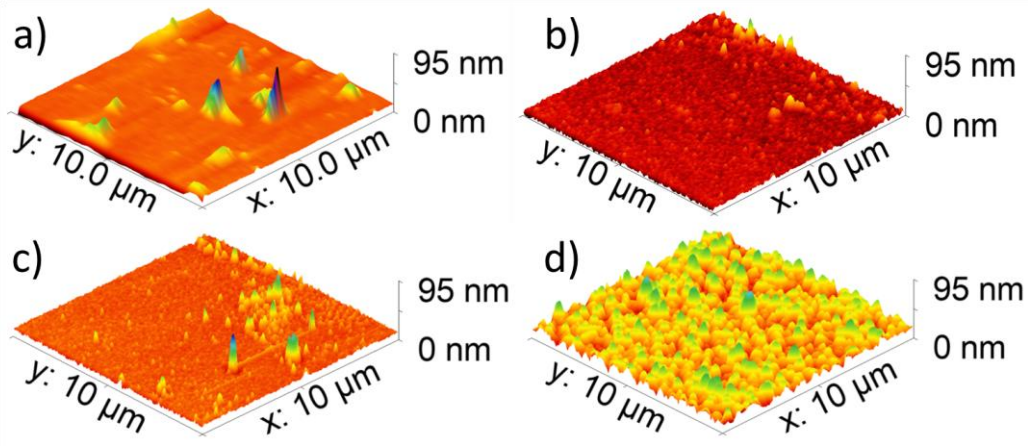


*Figure 5. Topography images obtained using AFM microscope for the samples a) non-implanted, b) implanted with $d_1$ dose 2e16 ions/cm$^2$, c) implanted with $d_2$ dose 1e17 ions/cm$^2$ and d) implanted with $d_3$ dose 1e18 ions/cm$^2$.*

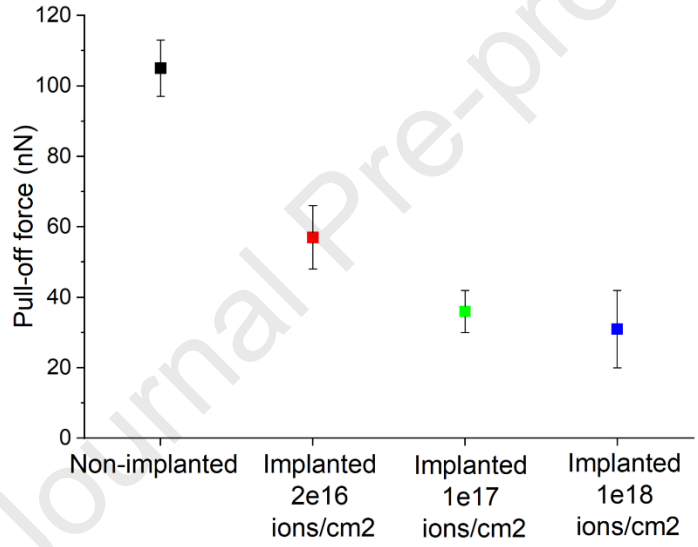


*Figure 6. Pull-off force measured on the implanted and non-implanted surfaces.*

### 3.3. Microstructure and phase composition

Figure 7 a-c presents a set of XRD diffractograms, comparing experimental data with theoretically calculated phases. Several binary nitrides were identified. According to the calculations, implantation with the lowest dose, $d_1$, led to the formation of two orthorhombic nitrides: $Ta_3N_5$ (space group Cmcm) and $Zr_3N_4$ (space group Pnma), as well as rocksalt-type TaN (space group $Fm\bar{3}m$) and tetragonal $Ti_2N$ (space group $P4_2/mnm$). On the other hand, an increase in the nitrogen dose resulted in the predominant formation of cubic nitrides, including TaN and ZrN (both rocksalt-type, space group $Fm\bar{3}m$), $Hf_3N_4$ (space group $I\bar{4}3d$), and $W_3N_4$ (space group $Pm\bar{3}m$). Additionally, traces of tetragonal $Nb_4N_5$ (space group I4/m) and orthorhombic $Ta_3N_5$ (space group Cmcm) were detected. The phases identified in the sample implanted with dose $d_3$ were similar to those found for dose $d_2$, with one exception: instead of

ZrN, cubic $Zr_3N_4$ (space group $\bar{I}43d$) was observed. The phase content calculated using Match! 3 software (Fig. 7 d) indicates that ion implantation can both promote the formation of the crystalline phase - as shown by the increased crystalline content in the sample implanted with the lowest dose ($d_1$) - and induce the formation of the amorphous phase, as evidenced by the reduced crystalline content in the samples implanted with higher doses ($d_2$ and $d_3$), likely due to defect creation caused by the process.

Both SAED patterns taken from approximately 50 nm from the sample surface (Fig. 8 a-c) and the XRD spectra alongside the phase content presented in Figure 7 indicate that the dominant structural component of the samples remains amorphous after ion implantation. At the same time, XRD revealed the presence of several crystalline phases, suggesting that the implantation process promotes partial nanocrystallization and binary nitride formation. A comparison of the spectra suggests that the implantation process may slightly alter the atomic structure of metallic glasses, creating small crystalline domains. SAED patterns showed the evidence of lattice fringes and diffraction spots that would also indicate the presence of some crystalline phases. For samples implanted with doses $d_1$ and $d_3$ the diffraction spots are clearly visible, for sample implanted with $d_2$ dose the spots can also be detected after closer examination (white arrows on figure 8-b). The weak contrast of the diffraction spots can be explained by the fact that nanocrystallites formed at this dose are both very small and sparsely distributed. Being embedded in a heavily disordered amorphous matrix, their contribution to the overall diffraction pattern is strongly reduced and partially masked by diffuse scattering. This results in spots of much lower intensity compared to those observed for $d_1$ and $d_3$ doses.

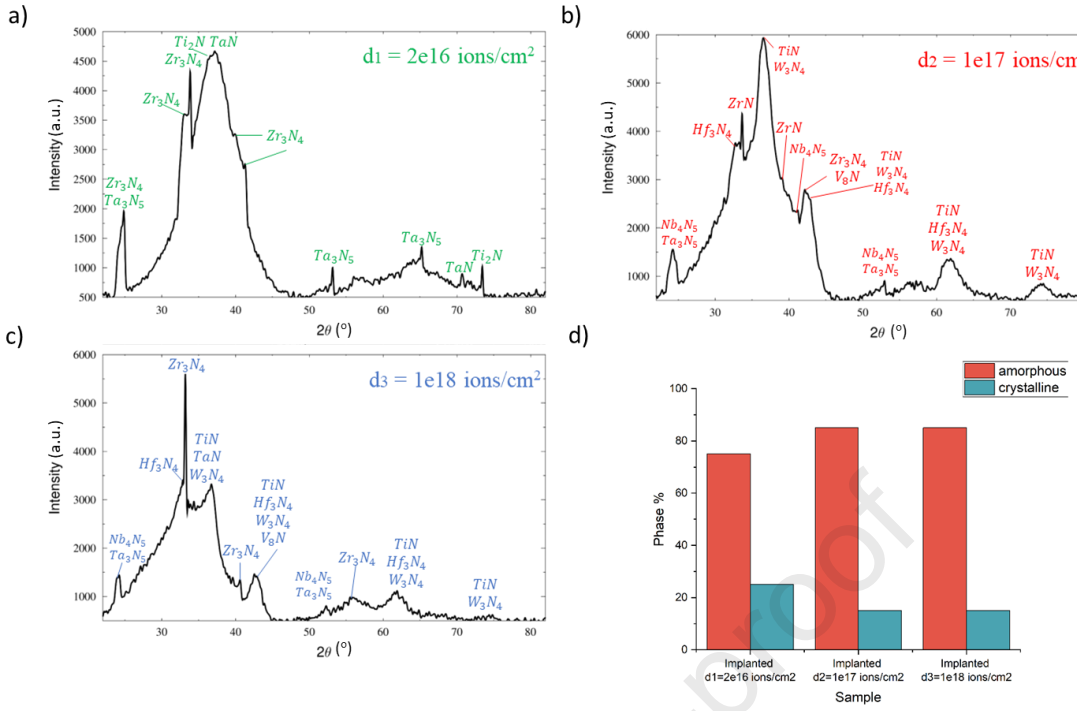


*Figure 7. a,b,c - XRD patterns of the as-deposited and nitrogen-implanted films. Reference peak positions for selected nitrides and metallic phases were simulated using VESTA. d - phase content in implanted samples obtained with Match! 3*

Figure 8 d-l presents TEM-HAADF micrographs of all implanted samples (d–f), accompanied by nitrogen EDS maps (g–i) and close-up images of the implanted layers (j–l). For the lowest dose ($d_1$), no significant changes in morphology or nitrogen distribution were observed (d, g, j), indicating minimal structural modification. Implantation with dose $d_2$ resulted in the formation of a well-defined nitrogen-rich zone at a depth between ~60 and 150 nm (e, h), which is in good agreement with SRIM simulations. In contrast, the highest dose ($d_3$) led to severe modifications in the microstructure (f, i), including the appearance of a porous-like layer near the surface, redistribution of elements and pronounced bright contrast in the HAADF image (l). The bright areas observed near the surface in HAADF images can be attributed to a combination of factors. Nitrogen implantation likely results in the formation of nitrides, such as HfN, ZrN, or TiN, which consist of elements with high atomic numbers. These nitrides strongly scatter electrons, producing a bright Z-contrast in the HAADF images. The implantation process may also induce local segregation of heavier elements like Hf, Ta, or W near the surface. These elements, with their higher atomic numbers, further enhance the scattering intensity. The implantation also modifies the atomic structure, potentially increasing the local atomic density and increasing stress near the surface, which contributes to the brighter contrast. Finally, nitrogen implantation creates a compositional gradient in the material, with a higher nitrogen concentration near the surface. This higher nitrogen content may interact with specific elements to form nitrogen-rich or denser regions, which also appear brighter in HAADF contrast. This observations are further confirmed with the results of EDS

mapping of all elements present in the samples (Fig. 9). For $d_1$ dose a fairly homogenous structure was obtained (Fig. 1 SI) and for $d_2$ dose barely visible segregation of elements was observed. On the other hand, a higher tantalum and hafnium content near the surface can be observed for $d_3$.

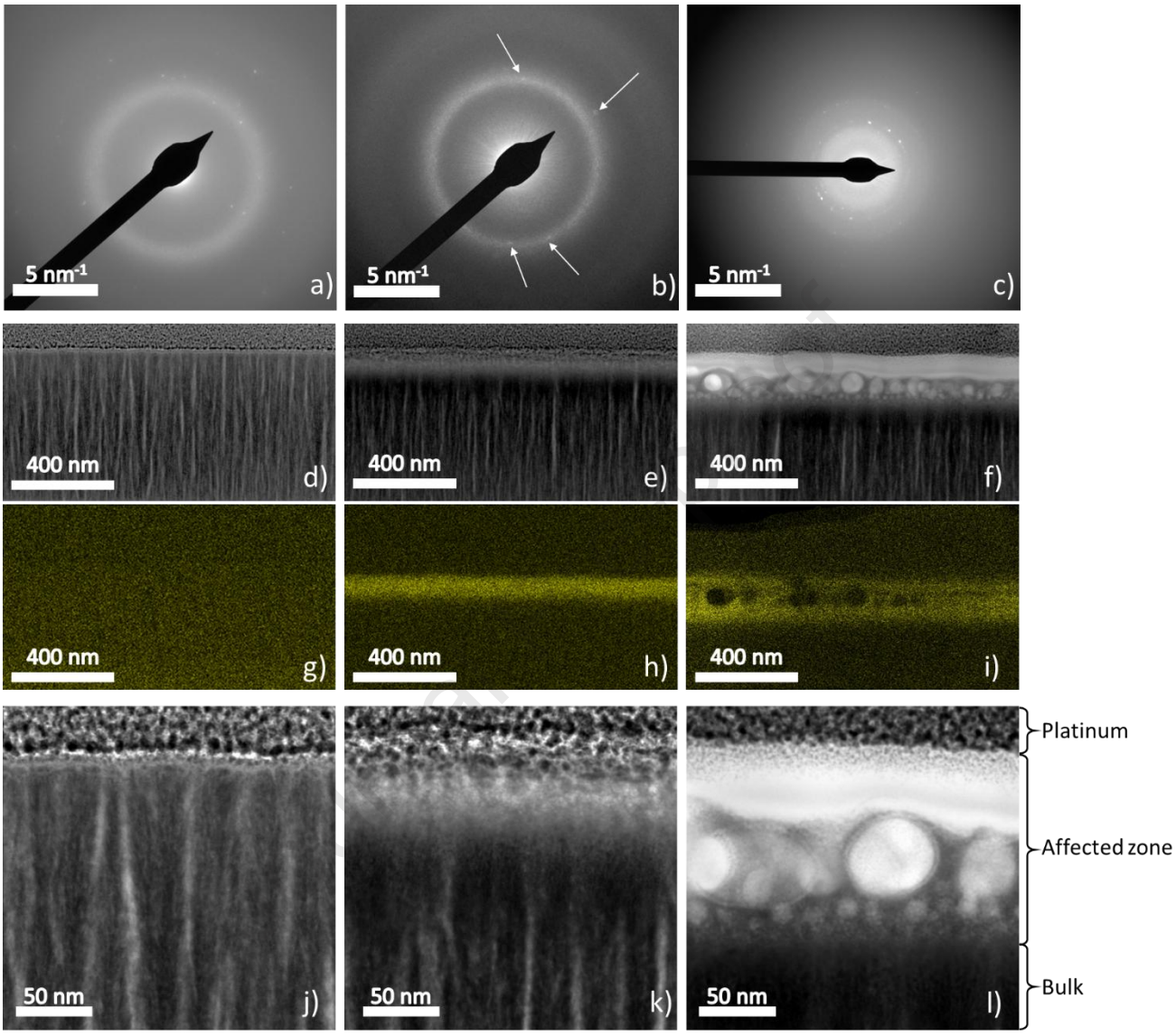


Figure 8. TEM diffraction patterns (a–c), cross-sectional HAADF-TEM images (d–f), nitrogen EDS maps (g–*i*) and high-magnification images (j-l) of implanted samples with increasing nitrogen doses: $d_1$, $d_2$, and $d_3$, respectively. A nitrogen-rich zone is visible for $d_2$, while $d_3$ shows significant microstructural changes and pore formation near the surface. Bright contrast in HAADF images (especially in i) is attributed to the formation of heavy-element nitrides, element segregation, and implantation-induced densification.

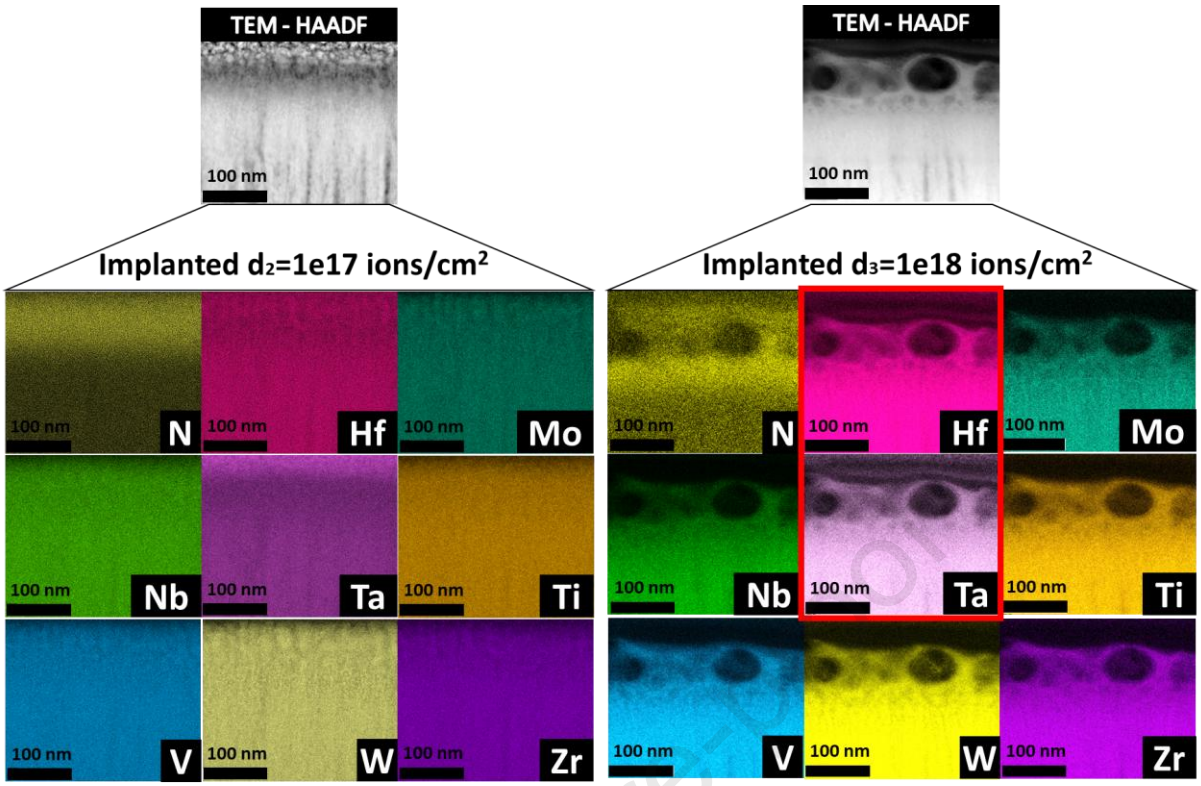


*Figure 9. TEM-HAADF images and EDS element mapping across the cross-sections of HfMoNbTaTiVWZr high-entropy TFMG samples implanted with 1e17 ions/cm$^2$ dose and 1e18 ions/cm$^2$ dose; distinctive hafnium and tantalum distribution marked with a red bracket.*

### 3.4. Mechanical characterization and wear resistance measurements

Indentation measurements were conducted to determine the hardness and wear resistance of the samples (Fig. 10). Fig. 10a shows an example result of the multicycle indentation experiment and in Fig. 10b, hardness vs indentation depth plots for all the investigated samples are presented. It can be observed that the sample implanted using 1e17 ions/cm$^2$ dose exhibits a large increase in hardness up to 20 GPa for a depth of around 25 nm. This sample is also characterized by the largest H/E and $H^3/E^2$ values (Fig. 10c). Conversely, the highest implantation dose introduced more defects into the structure, resulting in severe deterioration of properties. Hardness changes observed as a function of depth for a sample implanted with dose $d_2$ can be correlated to dpa. Fig 10d illustrates that while the overall trends of the curves are comparable, the reduction in hardness transpires more rapidly compared to the dpa curve. This shift can be attributed to several factors. First, recrystallization or stress relaxation near the surface may reduce hardness more rapidly than the accumulation of damage levels, particularly in regions of high implantation-induced stress. Additionally, as TEM shows, ion implantation caused segregation of elements, altering the chemical composition near the surface and affecting hardness disproportionately compared to dpa levels. Chemical composition gradients induced by ion implantation, particularly the formation of phases such as nitrides or enrichment with heavier elements,

can modify the local microstructure and influence hardness independently of radiation damage. The formation of various defects, such as vacancies and interstitials, which migrate and recombine differently depending on depth, may also contribute to this discrepancy. Notably, nanoindentation measures the material's response from a depth approximately 10 times greater than the indentation depth, integrating effects from a broader region and capturing contributions from areas with lower damage, potentially leading to an overall lower hardness reading compared to the localized damage levels indicated by dpa. These combined effects explain the observed rapid reduction in hardness relative to the dpa curve. It should be also noted that due to the self-similar shape of the dpa profile governed by Eq. (1), only one representative dpa - hardness correlation is shown in the main text. Additional plots for other fluences are provided in the Supplementary Information (Fig. S2).

The tribological behavior of the films was assessed using the scratch test, and the measured friction coefficients and penetration depths are shown in Fig. 11. The sample implanted with dose $d_2$ exhibited the best wear resistance, consistent with the hardness results, as it showed both the lowest coefficient of friction and the smallest penetration depth. The $d_3$ sample, on the other hand, displayed the highest penetration depth, which is associated with its porous microstructure. Such structural weakening decreases the surface load-bearing capacity, allowing deeper tip penetration during scratching. Importantly, all implanted samples demonstrated lower friction coefficients compared to the virgin film, which can be explained by reduced adhesion forces (confirmed by AFM, Fig. 6) that diminish the adhesive component of friction. Moreover, the virgin sample exhibited sudden drops in penetration depth caused by film delamination (see Fig. S3 in Supplementary Information). Since the film–substrate interface lies far beneath the implantation-affected region, this effect is attributed to differences in stress distribution between implanted and non-implanted films.

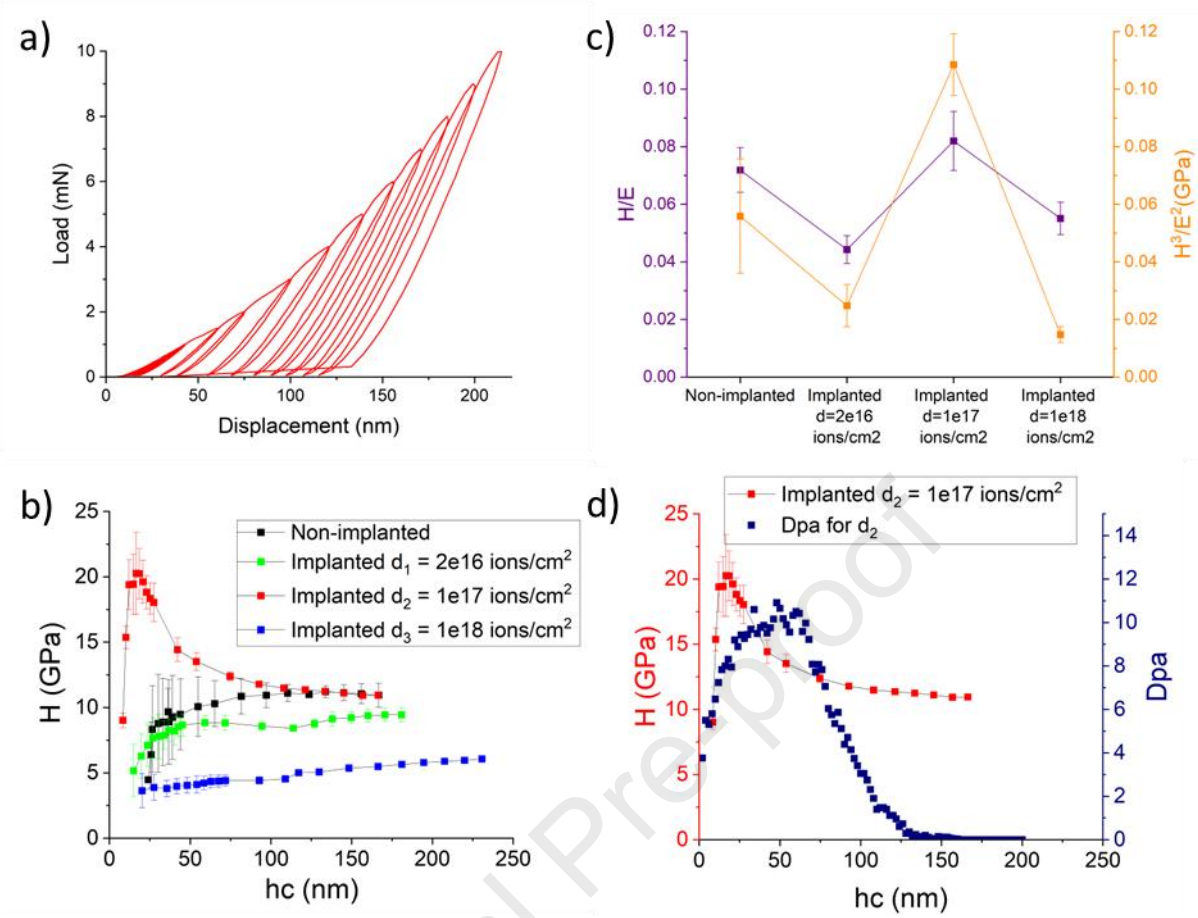


*Figure 10. a) Characteristic load-displacement curve for the sample implanted with dose 1e17 ions/cm$^2$ b) Measured hardness of implanted and non-implanted samples c) H/E and H$^3$/E$^2$ indexes obtained from indentation measurements; lines connecting the points are so called "guide for an eye" d) Correlation of hardness and dpa curves.*

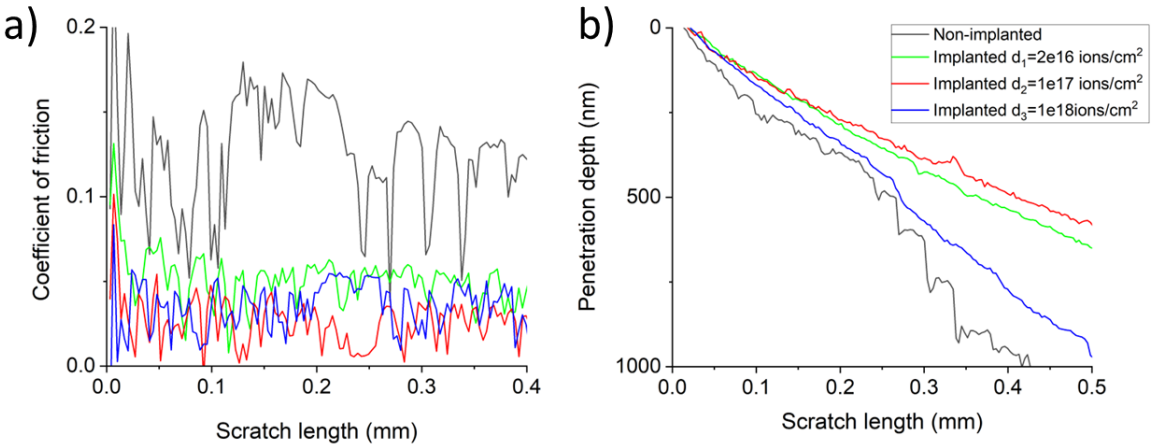


*Figure 11. a) Coefficients of friction calculated by scratch tester software and b) penetration depth measured by the scratch tester.*

Finally, table 5 presents nanoindentation toughness measurements results. They include only the implanted samples on which brittle fracture was observed. The non-implanted sample as well as sample implanted with the lowest dose $d_1$ shows a plastic behavior (figures 12a,b) - cracks around the imprint do not form – which is in line with previous observations [14]. Furthermore, the $K_{IC}$ toughness parameter was lower for the $d_2$ sample, which also exhibited the highest hardness, than for the $d_3$ sample. Ion implantation often generates residual stresses near the surface, which can amplify the tendency for crack initiation and propagation. In materials such as RHEMG, where toughness relies heavily on the amorphous or glassy matrix accommodating strain, the introduction of implantation-induced defects and microstructural changes, such as nitrides or segregation of heavier elements, can severely compromise these mechanisms, favoring brittle failure over plastic flow. The increase in hardness due to ion implantation also correlates with a reduction in the material's ability to absorb mechanical energy, making it more prone to brittle fracture under stress.

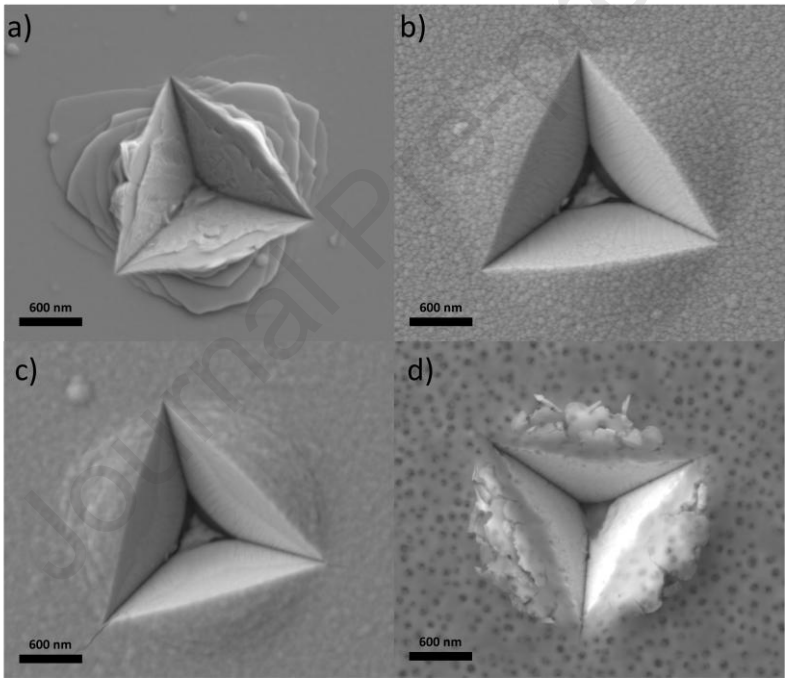


Figure 12. SEM images of imprints made during nanoindentation toughness measurements for samples: a) non-implanted b) implanted with $d_1$ c) implanted with $d_2$ and d) implanted with $d_3$ dose

*Table 4. $K_{IC}$ obtained from nanoindentation toughness measurements*

| Sample | Average E [GPa] | Average H [GPa] | c [µm] | $K_{IC}$[Mpa$\sqrt{m}$] |
|---|---|---|---|---|
| **Non-implanted** | 132.90±8.00 | 9.62±1.96 | 0 | - |
| **Implanted 1e17 ions/cm$^2$** | 158.44±13.88 | 8.28±1.09 | 0 | - |
| **Implanted 1e17 ions/cm$^2$** | 178.81±27.87 | 14.89±3.93 | 4.74±0.07 | 3.78±0.08 |
| **Implanted 1e18 ions/cm$^2$** | 87.94±19.69 | 4.76±0.8 | 4.04±0.10 | 5.99±0.23 |

## 4. Discussion

Nitrogen ion implantation significantly altered the microstructure, mechanical properties, and surface characteristics of the investigated material. It led to the formation of various nitride phases, changes in elemental distribution and increased surface roughness at higher doses. The mechanical properties were also affected, with moderate doses improving hardness and wear resistance, while excessive implantation introduced defects that reduced material performance. However, nitrogen ion implantation has not led to the formation of high entropy nitride even in the form of small inclusions. According to Fig. 13, the XRD diffractograms show no peaks corresponding to the theoretically determined diffraction pattern of (HfMoNbTaTiVWZr)N.

A closer examination of the microstructural changes reveals that elemental redistribution played a crucial role in nitrogen ion implantation induced modifications. Specifically, qualitative EDS analyses and microstructural characterization indicated an increased concentration of tantalum and hafnium near the surface of the sample, particularly above the implanted layer and within the porous zone of the sample implanted with a dose 1e18 ions/cm$^2$. This accumulation can be attributed to the high affinity of these elements for nitrogen, which promotes the preferential formation of tantalum nitride (TaN) and hafnium nitride (HfN) at the surface. The strong chemical interaction between nitrogen and these metals likely drives their atoms toward the nitrogen-rich regions near the surface. Additionally, both Ta and Hf are relatively large atoms, and their migration toward the surface can be facilitated by energy and momentum transfer during ion implantation. The thermodynamic stability of tantalum and hafnium nitrides further reinforces the tendency for these elements to segregate at the surface, where they can form stable nitride phases [27]. Interestingly, titanium also has a high affinity for nitrogen, but no significant segregation at the surface was observed in this study. This could be due to competing interactions among multiple elements within the high-entropy metallic glass matrix, which may limit titanium's mobility compared to tantalum and hafnium. A possible explanation for this effect is the sluggish diffusion phenomenon, one of the core effects of high-entropy alloys. The presence of multiple principal elements in the metallic glass matrix likely increases atomic-scale friction, which can hinder the diffusion of certain elements, such as titanium, despite their thermodynamic tendency to react with nitrogen. Further investigation is required to determine whether kinetic or thermodynamic factors dominate this phenomenon. Accurate depth-resolved composition measurements would require techniques such as RBS or ERDA instead of rather qualitative EDS results.

The preferential segregation of tantalum and hafnium has further practical relevance for extreme-environment applications. Both Ta and Hf form thermodynamically stable nitrides with very high melting points, which can act as diffusion barriers and improve resistance to nitrogen loss, oxidation, or structural relaxation during long-term exposure at elevated temperatures. Their enrichment

464 at the surface may therefore stabilize the nitrogen-rich modified layer and limit degradation mechanisms
465 such as grain coarsening or stress-assisted structural relaxation. These effects may contribute to the
466 hardness fluctuations observed at shallow penetration depths, reflecting a competition between local
467 hardening (TaN/HfN formation) and microstructural weakening in regions containing voids or
468 compositional discontinuities. From a tribological perspective, the presence of TaN and HfN can locally
469 increase load-bearing capacity and reduce adhesive wear, as these nitrides are both hard and chemically
470 stable. However, excessive segregation - especially when combined with implantation-induced porosity
471 - may also introduce compositional inhomogeneities that lower fracture toughness and promote crack
472 initiation under high contact stresses. Thus, the balance between beneficial hard nitride formation and
473 detrimental structural discontinuities is critical for optimizing the material's long-term behaviour in
474 high-temperature or high-load tribological environments

475 It is worth to note that the sample implanted with 1e18 ions/cm² exhibited a porous-like structure
476 similar to those observed in materials subjected to helium ion implantation, a process commonly used
477 to simulate irradiation-induced damage. According to the literature several mechanisms may contribute
478 to the observed porosity. For example, Liu et al. investigated helium ion implantation effects on CLAM
479 steel and reported phenomena such as blistering and swelling, which can occur under high ion doses or
480 when the sample surface is uneven [28]. Similarly, Dhara et al. observed nanoblistering in GaN
481 implanted with $Ga^+$ ions, attributing it to the accumulation of defects, displacement damage, and inert
482 gas retention, which led to the formation of voids and bubbles [29]. Excessive defect accumulation due
483 to high ions implantation doses introduces a substantial number of point defects and vacancies, which
484 can aggregate into voids. Furthermore, in the case of nitrogen ions the precipitation of nitrides such as
485 TaN and HfN may create local volume expansion, leading to stress buildup and subsequent void
486 formation. Above mentioned, preferential migration of elements such as tantalum and hafnium toward
487 the surface may contribute to local compositional inhomogeneities and phase separation, weakening the
488 material and promoting porosity. At high doses, increased momentum transfer from nitrogen ions may
489 enhance sputtering effects, further modifying the surface topology and promoting pore formation.

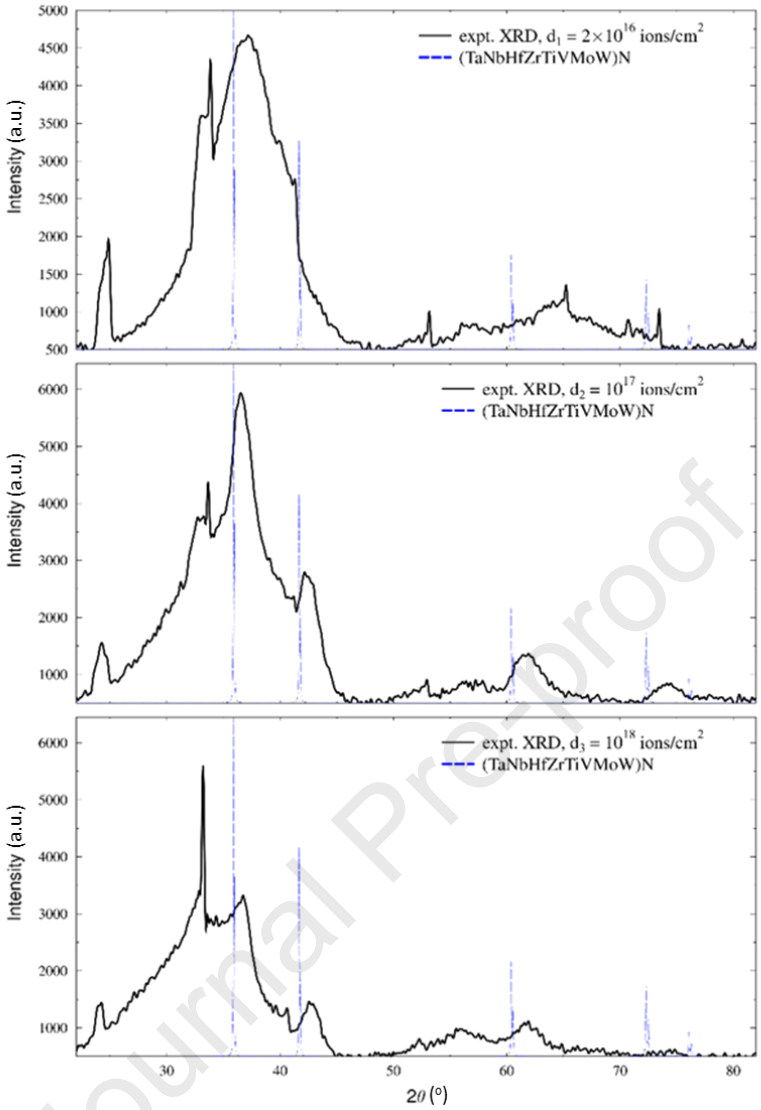


*Figure 13. XRD patterns of high entropy nitride (HfMoNbTaTiVWZr)N, calculated with VESTA software, compared to experimental XRD patterns for implanted samples*

The microstructural modifications induced by nitrogen implantation - such as nitride precipitation, elemental redistribution, and porosity formation - strongly influence the mechanical behavior of the investigated metallic glass. At the optimal fluence ($d_2$), nitrogen incorporation leads to atomic-scale structural rearrangements within the amorphous matrix, including densification and short-range-order modifications that improve local packing efficiency and hinder shear-transformation-zone activation. Together with the formation of fine nitride clusters and moderate implantation-induced stresses, these effects result in localized hardening and improved wear resistance. In contrast, the highest implantation dose ($d_3$) produces a fundamentally different response. Pronounced Ta and Hf segregation generates chemically and mechanically heterogeneous regions, while extensive porosity reduces the effective load-bearing cross-section and introduces stress concentrators. In metallic glasses, plastic flow occurs exclusively through localized shear banding; however, such heterogeneities decrease the critical

stress required for shear-band initiation and destabilize their propagation, promoting premature localization and runaway softening. The combined effect of segregation and porosity thus outweighs the beneficial strengthening observed at $d_2$ and leads to the severe reduction in hardness and in the H/E and $H^3/E^2$ ratios shown in Fig. 10.

While nitride formation can enhance wear resistance by increasing hardness, excessive porosity degrades mechanical durability by facilitating localized damage under mechanical loading. This interpretation is consistent with the indentation-derived mechanical indicators: the H/E ratio, associated with elastic strain to failure[30], and the $H^3/E^2$ ratio, reflecting resistance to plastic deformation [31]. Higher values of these parameters correlate with improved wear resistance, yet their decrease at $d_3$ confirms the detrimental effect of high-fluence implantation. Due to measurement uncertainties, indentation-based wear predictions are not fully conclusive, necessitating direct scratch testing to evaluate the tribological performance.

Interpretation of friction behavior also requires consideration of the coating's geometry and surface characteristics. The measured surface roughness (RMS ~1.8 nm for the as-deposited film) remained nearly unchanged after implantation, indicating that topography did not significantly affect the friction response. Moreover, the coating thickness (~1 μm) was sufficient to suppress substrate effects during testing. Therefore, the observed reduction in friction coefficient after implantation (from ~0.23 to ~0.17) can be primarily attributed to implantation-induced modifications of surface chemistry and mechanical properties - such as near-surface hardening - rather than to geometrical or roughness-related artefacts. The stable surface morphology and adequate thickness ensure that the tribological measurements predominantly reflect intrinsic material behavior.

Finally, the hardness measurements of the nitrogen ion-implanted sample with the $d_2$ dose were compared with those obtained for a thin film of (HfMoNbTaTiVWZr)N deposited by magnetron sputtering in our previous work [14] (Fig. 14a). The magnetron-sputtered sample, characterized by a nanocrystalline structure and a uniform nitrogen distribution across its cross-section, exhibited consistently high hardness throughout the depth. In contrast, the nitrogen-implanted sample retained mainly its amorphous structure, as confirmed by TEM and XRD, and exhibited a modified surface region enriched in nitrogen without forming a continuous crystalline nitride phase. Interestingly, at the initial stage of indentation, the implanted sample exhibited approximately twice the hardness of the sputtered sample (Fig. 14b), demonstrating that nitrogen implantation can effectively enhance surface hardness even without inducing a full phase transformation. The hardness–depth profiles of the two samples differ significantly, reflecting their distinct nitrogen distributions and structural features. In the magnetron-sputtered coating, hardness gradually increases with indentation depth, likely due to the uniform composition and nanocrystalline structure of the high-entropy nitride layer. In contrast, the implanted sample shows a rapid rise in hardness within the nitrogen-enriched surface region, followed by a decline

beyond the peak, as the indenter penetrates into the underlying amorphous matrix that was not modified by implantation. This behavior is consistent with the presence of a relatively thin, hardened zone formed near the surface, where the hardness enhancement originates mainly from implantation-induced modifications within the amorphous matrix, while the small volume fraction of nitride nanocrystallites contributes only secondarily. Surface roughness introduced by implantation may also influence the near-surface indentation response, particularly at very shallow depths (<20 nm), where even slight topographical variations can lead to local underestimation of hardness. In amorphous materials, such deviations from the classical indentation size effect are not uncommon and may also arise from additional factors, including limited accuracy in contact area estimation due to tip rounding, instrument noise and thermal drift. Furthermore, time-dependent viscoplastic deformation of the amorphous matrix may contribute to a reduction in measured hardness at very low penetration depths. As a result, the observed decrease in hardness below 20 nm should be interpreted with caution and considered an artifact of shallow-depth testing, rather than an intrinsic material response.

The maximum hardness values further emphasize the structural differences between the two surface modifications: while the sputtered nitride coating reaches ~27 GPa, the implanted sample achieves ~20 GPa. This discrepancy highlights the contrasting nature of the surface engineering approaches - uniform nitride formation via reactive sputtering versus compositional and structural gradients introduced by nitrogen ion implantation into an amorphous alloy [14]. It is also important to note that retaining the amorphous structure provides several intrinsic advantages that distinguish the implanted layer from the reactively sputtered nitride coating. Amorphous refractory high-entropy alloys exhibit superior resistance to irradiation-induced defect accumulation and structural degradation, as demonstrated previously for the same system in Ref. [12]. The absence of grain boundaries eliminates pathways for accelerated diffusion, oxidation or embrittlement, which is particularly beneficial for applications in extreme environments. Furthermore, the chemically and structurally disordered amorphous matrix can accommodate local stresses more uniformly than a nanocrystalline nitride, reducing the likelihood of crack initiation. Therefore, achieving surface hardening while preserving the amorphous state offers a complementary and technologically meaningful alternative to full nitride formation.

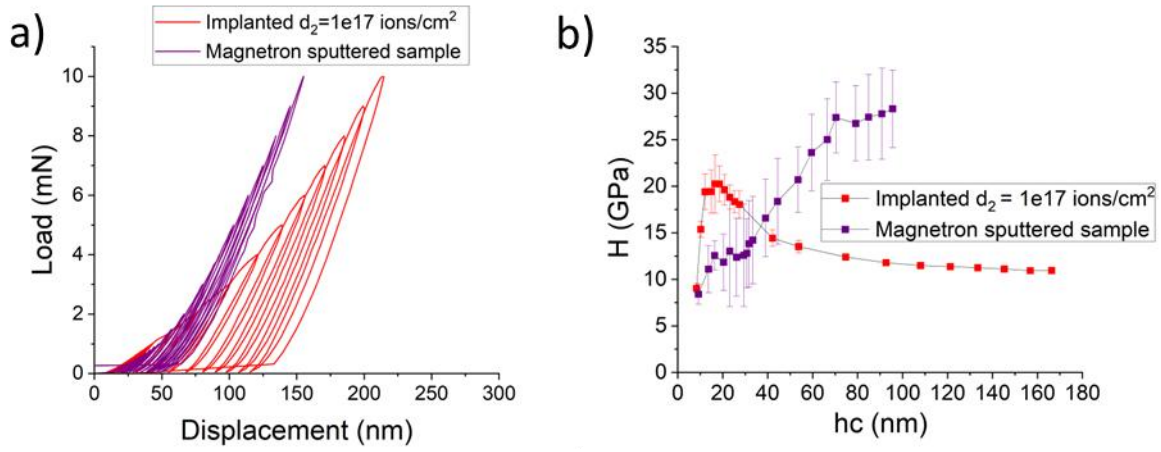


Figure 14. a) Load-displacement curves for implanted with $d_2$ dose and magnetron sputtered sample b) measured hardness on both samples

## 5. Conclusions

In conclusion, the present work provides a comprehensive evaluation of nitrogen ion implantation as a method for modifying the surface and mechanical properties of a high-entropy metallic glass thin film. The key findings are summarized as follows:

- This study examined the effects of nitrogen ion implantation on an octonary high-entropy thin film metallic glass (HfMoNbTaTiVWZr), revealing significant surface modifications including binary nitride formation, local elemental redistribution and changes in surface roughness and adhesion, while maintaining a largely amorphous structure.
- Mechanical performance was highly dose-dependent, with the $d_2$ dose ($1\times10^{17}$ ions/cm²) yielding optimal results - hardness increased to ~20 GPa and wear resistance improved, as evidenced by the lowest friction coefficient; in contrast, the $d_3$ dose ($1\times10^{18}$ ions/cm²) introduced structural defects such as porosity and elemental segregation, degrading performance.
- Comparison with a magnetron-sputtered nanocrystalline (HfMoNbTaTiVWZr)N coating showed differing hardness-depth profiles: the ion-implanted film exhibited a peak near the surface, while the sputtered coating maintained uniform hardness, attributable to their respective structural characteristics.
- These findings confirm nitrogen ion implantation as an effective surface engineering approach for tailoring the mechanical and tribological properties of refractory high-entropy metallic glasses, with dose optimization critical to balancing enhancement and damage.

**CRediT authorship contribution statement**

Karolina Stępniak: Writing – original draft, Methodology, Investigation, Formal analysis, Visualization.
Farid Akhtar: Resources, Methodology, Writing – review & editing.
Kinga Jasiewicz: Investigation, Data curation, Methodology.
Neonila Levintant-Zayonts: Resources, Writing – review & editing,
Aleksandra Królicka – Investigation,
Dariusz M. Jarząbek – Investigation, Methodology, Writing - review & editing, Supervision, Funding acquisition, Conceptualization.

**Declaration of competing interest**

The authors declare that they have no known competing financial interests or personal relationships that could have appeared to influence the work reported in this paper.

**Declaration of Generative AI and AI-assisted technologies in the writing process**

During the preparation of this work the authors used ChatGPT 4o in order to improve the language and correct all the grammatical and spelling errors. After using this tool, the authors reviewed and edited the content as needed and take full responsibility for the content of the publication.

**Acknowledgments**

The authors acknowledge the support of the National Science Centre in Poland through Grant 2021/43/B/ST8/02895.

**References**

[1] A. Troglia, C. Leriche, M.L. van de Poll, C. Morscher, G.H. ten Brink, B.J. Kooi, B. Weber, R. Bliem, Bridging the gap between high-entropy alloys and metallic glasses: Control over disorder and mechanical properties of coatings, Mater Today Commun 41 (2024) 110604. https://doi.org/10.1016/J.MTCOMM.2024.110604.

[2] M.A. Tunes, V.M. Vishnyakov, Microstructural origins of the high mechanical damage tolerance of NbTaMoW refractory high-entropy alloy thin films, Mater Des 170 (2019) 107692. https://doi.org/10.1016/j.matdes.2019.107692.

[3] N. Neuber, O. Gross, M. Eisenbart, A. Heiss, U.E. Klotz, J.P. Best, M.N. Polyakov, J. Michler, R. Busch, I. Gallino, The role of Ga addition on the thermodynamics, kinetics, and tarnishing properties of the Au-Ag-Pd-Cu-Si bulk metallic glass forming system, Acta Mater 165 (2019) 315–326. https://doi.org/10.1016/j.actamat.2018.11.052.

[4] A. Jalali, M. Malekan, E.S. Park, R. Rashidi, A. Bahmani, G.H. Yoo, Thermal behavior of newly developed Zr33Hf8Ti6Cu32Ni10Co5Al6 high-entropy bulk metallic glass, J Alloys Compd 892 (2022) 162220. https://doi.org/10.1016/J.JALLCOM.2021.162220.

[5] Y. Chen, Z.-W. Dai, J.-Z. Jiang, High entropy metallic glasses: Glass formation, crystallization and properties, J Alloys Compd 866 (2021) 158852. https://doi.org/10.1016/j.jallcom.2021.158852.

[6] Z.K. Dehkordi, M. Malekan, M. Nili-Ahmadabadi, Superplastic formability of the developed $Zr_{40}Hf_{10}Ti5Al_{10}Cu25Ni_{10}$ high entropy bulk metallic glass with enhanced thermal stability, J Non Cryst Solids 576 (2022). https://doi.org/10.1016/j.jnoncrysol.2021.121265.

[7] Z. Savaedi, R. Motallebi, H. Mirzadeh, M. Malekan, Superplasticity of bulk metallic glasses (BMGs): A review, J Non Cryst Solids 583 (2022). https://doi.org/10.1016/j.jnoncrysol.2022.121503.

[8] Y. Jia, G. Li, H. Yang, X. Xie, P. Yang, L. Xu, Z. Wu, Y. Mu, K. Sun, S. Wu, X. Bian, Y. Jia, G. Wang, Achieving ambient superformability in a lightweight refractory medium-entropy alloy via stagewise adaptive microstructural buffers, J Mater Sci Technol 248 (2026) 212–223. https://doi.org/10.1016/J.JMST.2025.04.071.

[9] Y. Jia, G. Li, C. Ren, Y. Mu, K. Sun, S. Wu, X. Bian, Y. Jia, G. Wang, Substantially improved room-temperature tensile ductility in lightweight refractory Ti-V-Zr-Nb medium entropy alloys by tuning Ti and V content, J Mater Sci Technol 206 (2025) 234–247. https://doi.org/10.1016/J.JMST.2024.04.020.

[10] I. Ahmad, W. Akram, Introductory Chapter: Introduction to Ion Implantation, in: I. Ahmad (Ed.), Ion Implantation, IntechOpen, Rijeka, 2017. https://doi.org/10.5772/intechopen.68785.

[11] P.J. Tao, Y.Z. Yang, X.J. Bai, Z.X. Mu, Z.W. Li G. Q. and Xie, X.C. Chen, Study on implantation of Co ions in ZrCuNiAl bulk metallic glass, Surf Coat Technol 203 (2009) 1656–1659. https://doi.org/10.1016/j.surfcoat.2008.12.013.

[12] P. Jenczyk, D.M. Jarzabek, Z. Lu, E. Gadalińska, N. Levintant-Zayonts, Y. Zhang, Unexpected crystallographic structure, phase transformation, and hardening behavior in the AlCoCrFeNiTi0.2 high-entropy alloy after high-dose nitrogen ion implantation, Mater Des 216 (2022) 110568. https://doi.org/10.1016/J.MATDES.2022.110568.

[13] A.D. Pogrebnjak, O. V. Bondar, S.O. Borba, G. Abadias, P. Konarski, S. V. Plotnikov, V.M. Beresnev, L.G. Kassenova, P. Drodziel, Nanostructured multielement (TiHfZrNbVTa)N coatings before and after implantation of N+ ions (1018 cm−2): Their structure and mechanical properties, Nucl Instrum Methods Phys Res B 385 (2016) 74–83. https://doi.org/10.1016/J.NIMB.2016.09.002.

[14] S. Alvi, M. Milczarek, D.M. Jarzabek, D. Hedman, M.G. Kohan, N. Levintant-Zayonts, A. Vomiero, F. Akhtar, Enhanced Mechanical, Thermal and Electrical Properties of High-Entropy HfMoNbTaTiVWZr Thin Film Metallic Glass and its Nitrides, Adv Eng Mater 24 (2022). https://doi.org/10.1002/adem.202101626.

[15] Y. Alphan, M. Kaba, A. Motallebzadeh, H. Cimenoglu, Characterization of structural and mechanical properties of HfNbTaTiZr refractory high entropy alloy after gas nitriding, Intermetallics (Barking) 169 (2024). https://doi.org/10.1016/j.intermet.2024.108279.

[16] M. Yuan, X. Zhang, A.M.A. Saeedi, W. Cheng, C. Guo, B. Liao, X. Zhang, M. Ying, G.A. Gehring, Study of the radiation damage caused by ion implantation in ZnO and its relation to magnetism, Nucl Instrum Methods Phys Res B 455 (2019) 7–12. https://doi.org/10.1016/J.NIMB.2019.06.013.

[17] J.E. Sader, I. Larson, P. Mulvaney, L.R. White, Method for the calibration of atomic force microscope cantilevers, Review of Scientific Instruments 66 (1995) 3789–3798. https://doi.org/10.1063/1.1145439.

[18] H. Grzywacz, M. Milczarek, P. Jenczyk, W. Dera, M. Michalowski, D.M. Jarzabek, Quantitative measurement of nanofriction between PMMA thin films and various AFM probes, MEASUREMENT 168 (2021). https://doi.org/10.1016/j.measurement.2020.108267.

[19] P. Villars, Pearson's handbook: crystallographic data for intermetallic phases., (1985).

[20] D.A. Papaconstantopoulos, W.E. Pickett, B.M. Klein, L.L. Boyer, Electronic properties of transition-metal nitrides: The group-V and group-VI nitrides VN, NbN, TaN, CrN, MoN, and WN, Phys Rev B 31 (1985) 752–761. https://doi.org/10.1103/PhysRevB.31.752.

[21] https://next-gen.materialsproject.org/, (n.d.).

[22] W.C. Oliver, G.M. Pharr, Measurement of hardness and elastic modulus by instrumented indentation: Advances in understanding and refinements to methodology, J Mater Res 19 (2004) 3–20. https://doi.org/10.1557/jmr.2004.19.1.3.

[23] B.R. LAWN, A.G. EVANS, D.B. MARSHALL, Elastic/Plastic Indentation Damage in Ceramics: The Median/Radial Crack System, Journal of the American Ceramic Society 63 (1980) 574–581. https://doi.org/10.1111/j.1151-2916.1980.tb10768.x.

[24] D.S. Harding, W.C. Oliver, G.M. Pharr, Cracking During Nanoindentation and its Use in the Measurement of Fracture Toughness, MRS Proceedings 356 (1994) 663. https://doi.org/10.1557/PROC-356-663.

[25] M. Nastasi, J.W. Mayer, Ion Implantation and Synthesis of Materials, Springer Berlin Heidelberg, Berlin, Heidelberg, 2006. https://doi.org/10.1007/978-3-540-45298-0.

[26] E. Pitthan, V.P. Amarasinghe, C. Xu, T. Gustafsson, F.C. Stedile, L.C. Feldman, 4H-SiC surface energy tuning by nitrogen up-take, Appl Surf Sci 402 (2017) 192–197. https://doi.org/10.1016/J.APSUSC.2017.01.073.

[27] A. Hoshang Ramezani, S. Hoseinzadeh, A. Bahari, The Effects of Nitrogen on Structure, Morphology and Electrical Resistance of Tantalum by Ion Implantation Method, 28 (2018) 847–853. https://doi.org/10.1007/s10904-017-0769-4.

[28] P.P. Liu, Q. Zhan, Z.Y. Fu, Y.P. Wei, Y.M. Wang, F.M. Wang, S. Ohnuki, F.R. Wan, Surface and internal microstructure damage of He-ion-irradiated CLAM steel studied by cross-sectional transmission electron microscopy, J Alloys Compd 649 (2015) 859–864. https://doi.org/10.1016/j.jallcom.2015.07.177.

[29] S. Dhara, Formation, Dynamics, and Characterization of Nanostructures by Ion Beam Irradiation, Critical Reviews in Solid State and Materials Sciences 32 (2007) 1–50. https://doi.org/10.1080/10408430601187624.

[30] A. Leyland, A. Matthews, On the significance of the H/E ratio in wear control: a nanocomposite coating approach to optimised tribological behaviour, Wear 246 (2000) 1–11. https://doi.org/10.1016/S0043-1648(00)00488-9.

[31] S. Zang, Thin Films and Coatings: Toughening and Toughness Characterization, CRC Press, 2015. https://doi.org/10.1201/B18729-12/ADVANCED-HARD-COATINGS-ENHANCED-TOUGHNESS-RESISTANCE-CRACKING-SAM-ZHANG.

**Declaration of interests**

☐ The authors declare that they have no known competing financial interests or personal relationships that could have appeared to influence the work reported in this paper.

☒ The authors declare the following financial interests/personal relationships which may be considered as potential competing interests:

| |
|---|
| Dariusz Jarzabek reports financial support was provided by National Science Centre Poland. Dariusz Jarzabek reports a relationship with National Science Centre Poland that includes: funding grants. If there are other authors, they declare that they have no known competing financial interests or personal relationships that could have appeared to influence the work reported in this paper. |